

How Digital Correlation Affects the Fringe Washing Function in L-Band Aperture Synthesis Radiometry

Mark A. Fischman, *Member, IEEE*, Anthony W. England, *Fellow, IEEE*, and Christopher S. Ruf, *Fellow, IEEE*

Abstract—The phase coherence limitations of L-band digital correlation radiometry are investigated for receiver architectures that use low A/D converter resolution (1–3 bits). Statistical models and measurements of a 1.4 GHz digital radiometer system show that coarse quantization can cause excess fringe washing losses which degrade the spatial resolution capabilities in synthetic thinned array radiometry (STAR) implementations. For single-bit STAR, excess fringe washing is discernible immediately away from the boresight direction and, further from the center of the image, can result in as much as 2 dB loss in visibility information.

To accommodate low-bit correlators in remote sensing STAR, a novel band division correlation (BDC) processor is proposed. BDC improves the time-coherence of each correlated brightness signal while it also maintains the system bandwidth and noise-equivalent sensitivity of a conventional STAR radiometer. Analytical and numerical solutions are presented for the point spread function of a 27 m L-band STAR sensor to evaluate the band-slicing technique. The results show that with 4 subband channels, BDC improves swath edge resolution from 17.0 to 10.2 km and reduces correlation loss from 2.5 to 0.2 dB.

Index Terms—Analog-to-digital converters, digital correlator, soil moisture and ocean salinity, spatial resolution, synthetic thinned array radiometer, visibility function.

I. INTRODUCTION

SYNTHETIC thinned array radiometry (STAR) is emerging as a promising technology for satellite radiometers, especially those which operate at the low end of the microwave spectrum. The main benefit of STAR is that desirable spatial resolutions can be attained without the complexity of a filled aperture system. The concept behind aperture synthesis is not new, but has in fact been used extensively in radio astronomy since the 1950s for high resolution interferometric imaging and for spectroscopy of cosmic targets [1]. Within the last 15 years, there has been a strong interest in adapting these radio astronomy techniques to test their applicability for L-band (1.4 GHz) satellite-based observations of the Earth [2]—especially for retrieving soil moisture and ocean salinity data that would greatly enhance the accuracy of weather and climate models.

Researchers have experimented with both analog and digital receiver architectures as L-band STAR for Earth remote sensing has evolved toward larger, more complex array configura-

tions. The Electronically Steered Thinned Array Radiometer (ESTAR) was the first prototype to be developed for airborne demonstration; using a five-element, hybrid real/synthetic aperture scheme, and analog correlation electronics, ESTAR proved itself capable of recovering soil moisture information in field campaigns over watersheds in Arizona and Oklahoma [3], [4]. More recently, several organizations have been developing new L-band STAR instruments offering two-dimensional beam synthesis and a simpler, 1-bit digital correlator design which is more easily implemented within the limitations of today's technologies. For example, the Helsinki University of Technology is implementing a 36-element digital airborne STAR array, named HUT-2D [5]. Similarly, the European Space Agency (ESA) is currently in Phase B development of an 80-element, Y-shaped satellite array for its soil moisture and ocean salinity (SMOS) mission [6], [7].

One of the unique features of Earth remote sensing STAR is that the instrument requires a much wider field of view (FOV) than in the case of radio astronomy. While the statistical properties of low resolution digital correlators have been studied previously in astronomy applications [8], [9], [10], it has yet to be determined how quantization of the received brightness signals in Earth observing STAR affects the synthesized beam properties over a wide FOV. In this paper, we examine the imaging capabilities of advanced aperture synthesis instruments that employ digital correlation techniques. The impulse response of an L-band digital correlation radiometer—the building block in advanced sensors such as SMOS—will be examined in Sections II–IV to establish the relation between digitization and correlation loss. Section V introduces a novel processing technique for STAR correlators that enhances the spatial resolution capabilities over the FOV and offsets the loss of spatial resolution caused by quantization.

II. FRINGE WASHING PHENOMENON

STAR is comprised of antenna elements distributed in space to form a sparse array. The correlated pairs of received signals are the complex visibility functions, $V(n)$, which represent the spatial frequency components of the brightness scene T_B [11]. That is

$$V(n) = \int_{-1}^1 \frac{1}{\sqrt{1-\mu^2}} T_B(\mu) r_w(n, \mu) e^{-j\pi n \mu} d\mu \text{ for } n = 0, 1, \dots, N \quad (1)$$

where $\mu = \sin \theta$ is the direction sine of nadir angle θ , n is the separation between elements in half-wavelengths ($\lambda/2$), and r_w is the *fringe washing function*. Fringe washing describes a wors-

Manuscript received April 16, 2001; revised August 30, 2001.

M. A. Fischman was with the Radiation Laboratory, The University of Michigan, Ann Arbor, MI 48109-2122 USA. He is now with the Jet Propulsion Laboratory, California Institute of Technology, Pasadena, CA 91109 USA (e-mail: mafisch@mail1.jpl.nasa.gov).

A. W. England and C. S. Ruf are with the Radiation Laboratory, The University of Michigan, Ann Arbor, MI 48109-2122 USA (e-mail: england@umich.edu).

Publisher Item Identifier S 0196-2892(02)03265-5.

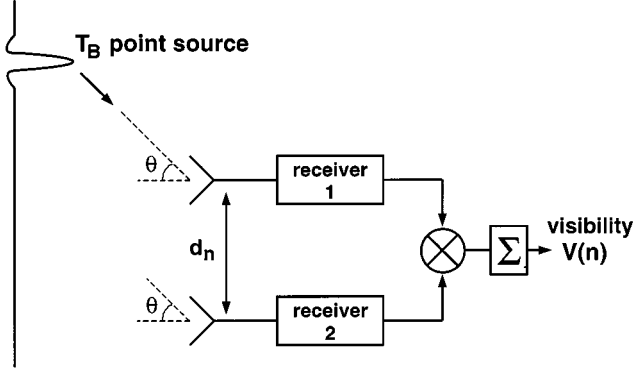


Fig. 1. Geometry for a correlation radiometer viewing a point source located at an angle θ away from the boresight direction. The antenna elements are physically separated by a distance d_n to sample one spatial frequency of the brightness scene.

ening in spatial resolution caused by decorrelation of the target signal as the synthesized beam is steered away from boresight. The decorrelation results from the nonzero system bandwidth, B , of the STAR sensor. At larger element spacings, the lag time between reception of a pair of brightness signals may approach or exceed the $1/B$ correlation time of the bandlimited noise processed by the radiometer. Visibility samples for these large spacings will incur a loss of correlation that causes degraded resolution in the reconstructed brightness image.

The fringe washing function for each correlator is related to the receiver bandpass characteristics through a Fourier transform [12]:

$$r_w(\tau) = F^{-1} \{H_1(f - f_0)H_2^*(f - f_0)\} \\ = e^{-j2\pi f_0 \tau} \int_{-\infty}^{\infty} H_1(f) H_2^*(f) e^{j2\pi f \tau} df \quad (2)$$

where τ is the time lag between the two received signals, H_1 and H_2 are the transfer function responses for the first and second receiver channels, and f_0 is the center (carrier) frequency of the system. If two analog receivers are assumed to exhibit identical rectangular bandpass characteristics:

$$H_{1,2}(f) = \begin{cases} 1, & \text{for } f_0 - \frac{B}{2} \leq |f| \leq f_0 + \frac{B}{2}, \\ 0, & \text{otherwise} \end{cases} \quad (3)$$

the tapering in fringe washing is ideally described by the sinc function

$$r_w(\tau) = \text{sinc } B\tau. \quad (4)$$

Referring to the geometry of the correlation radiometer in Fig. 1, where the elements are separated by a distance $d_n = n\lambda/2$, the lag time can be written as

$$\tau = \frac{d_n \mu}{c} = \frac{n\mu}{2f_0} \quad (5)$$

where c is the speed of light. Then the STAR fringe washing function in (1) becomes

$$r_w(n, \mu) = \text{sinc} \left(\frac{nB\mu}{2f_0} \right). \quad (6)$$

For large baselines, (6) shows that the sensitivity of a correlation radiometer in STAR will taper off as the pixel location moves away from the center of the FOV. The exact shape of the

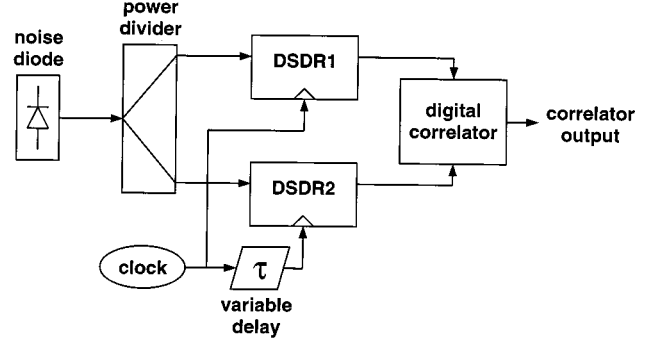


Fig. 2. Block diagram of the experimental setup for measuring fringe washing in a digital correlation radiometer.

fringe washing function is therefore a key performance figure for describing the spatial resolution and sensitivity capabilities in STAR.

III. CHARACTERIZATION OF A DIGITAL RADIOMETER

The preceding analysis considered fringe washing for the case of ideal analog correlation hardware. In digital STAR, signal quantization will introduce harmonics outside of the principal passband B and will alter the receivers' effective transfer functions, H_1 and H_2 , defined in (3). In this section, the fringe washing function will be measured directly using an L-band digital correlation radiometer to illustrate the effects of quantization.

A. The Correlation DSDR Prototype

We have designed a two-channel correlation radiometer prototype, operating at a center frequency of 1413.5 MHz, as a proof-of-concept for the direct RF sampling receiver concept [13]. This direct sampling digital radiometer (DSDR) is based upon the SPT7610 flash analog-to-digital converter, an emitter-coupled logic device that yields over 3 bits of sampling resolution at an analog input bandwidth of 1.4 GHz. A low noise RF front end provides 90 dB system gain and $B = 20$ MHz bandpass filtering before the A/D conversion. Short-term variations in the physical temperature of the front end electronics can cause gain fluctuations that degrade the radiometer's noise-equivalent sensitivity. To minimize these variations, the relative change in temperature of each front end is regulated to within 12 mK rms using a thermoelectric cooler and PID control circuitry. The digital cross-correlation between radiometer channels is processed with an Altera EPF10K20 field-programmable gate array (FPGA) and is sent to a PC data acquisition system.

B. Fringe Washing Measurements

End-to-end fringe washing measurements were performed with the correlation DSDR by injecting a pair of partially correlated noise sources into the two receiver channels, as shown in Fig. 2. For this experiment, the gain of each receiver channel is set to yield 3.3 bits (ten levels) of sampling resolution. The correlated power components are generated by a noise diode and Wilkinson power divider which splits the noise source between the two DSDR receivers. A decimation counter circuit and adjustable phase shifter are added to the DSDR2 clock

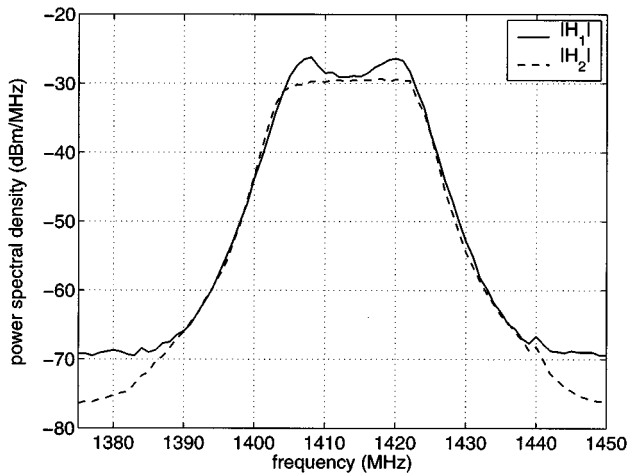


Fig. 3. Magnitude of the frequency response for DSDR1 and DSDR2 front end receivers (before digitization).

line to control the relative lag time τ between samplers; with these devices, τ can be incremented from -50 to $+50$ ns to simulate the correlation radiometer's response to a point source that moves across the FOV of two antenna elements. The phase shifter is fine tuned at each delay time setting to generate the peak correlation value (i.e., the envelope of the correlator's grating lobe pattern), and these data are normalized to unity at $\tau = 0$ to trace out the shape of the fringe washing function.

Fringe washing can also be estimated *before digitization* by redirecting the output signal from each front end to a spectrum analyzer. The magnitudes of H_1 and H_2 can then be found—at least in the analog domain—and applied to the relation in (2). The power spectral densities of the two analog output channels, measured over 1375–1450 MHz, are plotted in Fig. 3. Assuming a negligible phase imbalance between these channels, fringe washing is determined from the inverse Fourier transform of the magnitude product:

$$r_w(\tau) = e^{-j2\pi f_0 \tau} \int_{-\infty}^{+\infty} |H_1(f)| |H_2(f)| e^{j2\pi f \tau} df. \quad (7)$$

Fig. 4 shows the fringe washing results from the correlation DSDR experiments. The solid line is a plot of the expected (analog) response, derived from (7). Notice that this curve closely resembles a sinc function with a correlation length of 50 ns—which is exactly the result predicted by (4) for receivers having a 20 MHz rectangular bandpass response. The end-to-end fringe washing measurements, which are plotted alongside the sinc curve, take on a distinct and unforeseen characteristic, though. Instead of having a gradual, tapered response as τ moves away from zero, there is a sharp, almost triangular-shaped dropoff in the strength of the correlation. (There is also an asymmetry in the data that suggests some phase imbalance between the DSDR channels.) The correlation time and system bandwidth technically have not changed: on average, the first zero-crossings of the fringe washing data still intersect near ± 50 ns. Yet the strange compression of r_w observed in the time domain hints at the possibility that, in the frequency domain, the passband has been stretched beyond its original range. Section IV will explore how this phenomenon is linked to the digital receiver architecture.

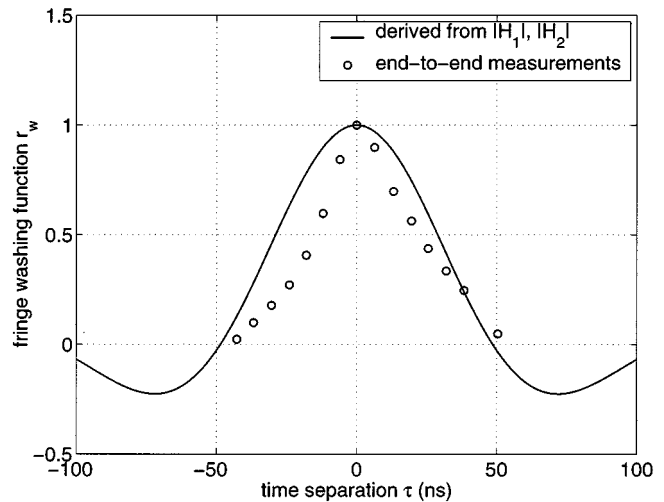


Fig. 4. Correlation DSDR fringe washing function determined from 1) the analog frequency response of each receiver and 2) direct (end-to-end) measurements at 3.3 bit resolution. The discrepancy between the two cases points to an unexpected loss of coherence for a finite time separation τ between digital samplers.

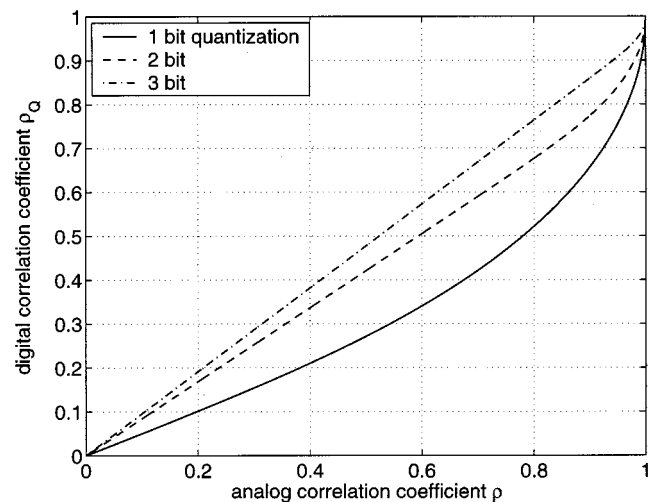


Fig. 5. Plot of the transfer function between analog and digital correlation coefficients for a range of bit resolutions.

IV. INTERPRETING DISCREPANCIES IN FRINGE WASHING

A. How Quantization Affects the Autocorrelation and Power Spectrum of a Signal

Fringe washing degradation can be understood by looking at the relation between the analog correlation coefficient ρ and its digital counterpart, ρ_Q , for a pair of brightness signals. Previously, we have derived this transfer function for arbitrary A/D converter resolution [13]. As a reference, the solutions at 1, 2, and 3 bit resolutions have been computed and plotted in Fig. 5. It is important to mention that by measuring DSDR's fringe washing function in Sections III with the variable delay line τ , we have in essence determined the envelope of the autocorrelation function for each quantized waveform (assuming that the receivers are matched). Because an autocorrelation is just a special case of the correlation between two random processes, that is, with identical signals that are separated in time, the *digitized*

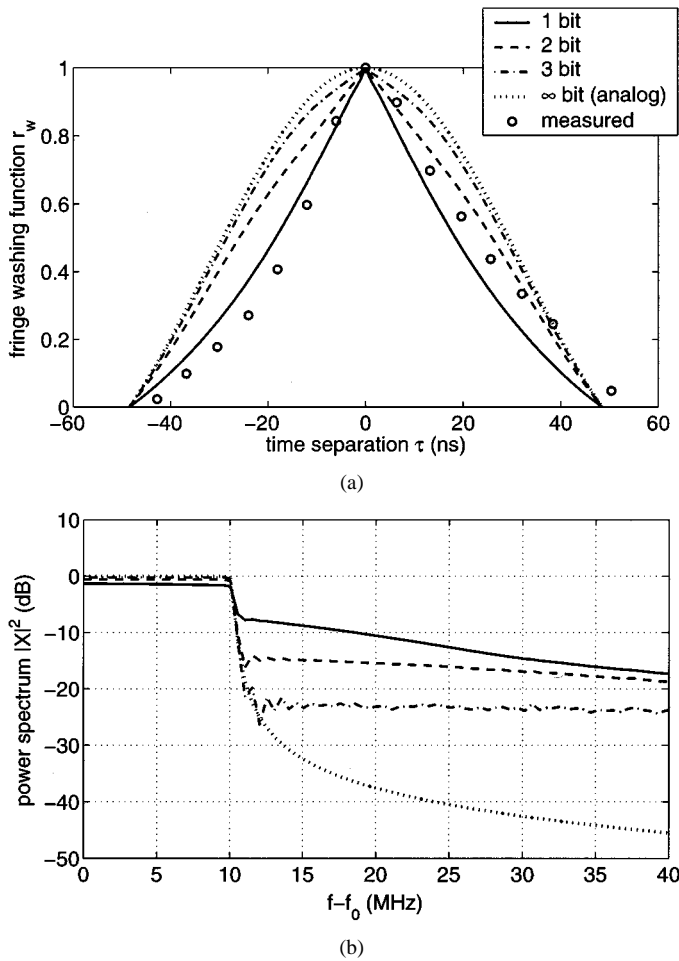


Fig. 6. (a) Fringe washing modeled over a range of bit resolutions. (Experimental data from DSDR are included for comparison.) (b) The corresponding power spectral densities of the quantized waveforms. At coarse resolution, nonlinearities in the A/D conversion cause the spectrum to be spread over a range of frequencies (*bandwidth spreading*).

fringe washing function can readily be found by plugging the analog solution from (4) into the ρ - ρ_Q transformation.

The nonlinear relation between ρ and ρ_Q in Fig. 5 is a cause of the peculiar distortion seen in DSDR's fringe washing function. In physical terms, A/D conversion is an inherently nonlinear operation, and as such, it can create out-of-band harmonics that extend beyond the principal passband B of the receiver. As quantization resolution is decreased, more energy is transferred out of the main passband and is spread over a broad range of frequencies. This *bandwidth spreading* phenomenon causes the correlation between the two digital receiver channels to become contracted in the time domain.

If a smoothly varying (analog) sinc function is applied to any of the nonlinear ρ - ρ_Q transformations in Fig. 5, a sharp, non-differentiable peak is generated at $\tau = 0$. Furthermore, because the change in ρ_Q with respect to ρ is greatest for correlation values near 1, the rolloff in fringe washing will be most severe in the neighborhood of small τ . (This also happens to correspond to the area immediately away from the boresight direction in aperture synthesis radiometry.) Fig. 6(a) shows the ideal fringe washing function described by (4), along with the transformed fringe washing functions for 1–3 bit resolutions. As the number

of bits decreases, the loss of coherence over $0 < \tau < 1/B$ becomes worse, and the shape of the predicted fringe washing function begins to resemble the curve measured with DSDR.

The power spectral densities of the quantized signals are found by applying a Fourier transform to each autocorrelation function [see Fig. 6(b)]. Here the increase in “bandwidth spreading” becomes obvious as bit resolution is reduced. While the physics behind this result is not surprising, it has important ramifications for digital STAR, which must be able to maintain signal coherence over a wide FOV.

B. Implications for STAR Correlators Having Coarse Resolution

Because fringe washing depends on the bandpass spectrum but not on the center frequency f_0 , the analysis presented for the L-band DSDR is just as relevant for similar radiometer systems that mix down to an intermediate frequency before digitization. The most noteworthy example is the L-band SMOS aperture synthesis array mentioned earlier. SMOS relies on a 1-bit IF sampling scheme to minimize design complexity in the A/D converter and digital correlator sections. But 1-bit quantization is also the coarsest possible resolution and, as seen in this study, the most severe in terms of coherence loss.

Recognizing that the bandwidth spreading problem may impact spatial resolution performance, it is useful to look at how a fixed 1-bit correlation radiometer will further alter fringe washing. This type of receiver uses a simple two-level comparator (signed operator) to convert from an analog signal x to digital signal \hat{x} :

$$\hat{x} = \begin{cases} +\frac{1}{2}, & \text{if } x \geq 0 \\ -\frac{1}{2}, & \text{if } x < 0. \end{cases} \quad (8)$$

For this special case, there exists a closed form solution for ρ_Q known as the Van Vleck relationship [8]:

$$\rho_Q = \frac{2}{\pi} \sin^{-1} \rho. \quad (9)$$

By setting ρ equal to the ideal analog fringe washing function, the corresponding fringe washing pattern of the digital correlator can be found. The relative change in gain between ideal and quantized cases defines the *excess coherence loss*

$$\text{excess } CL = \frac{r_w(\text{ideal})}{r_w(1\text{-bit})} = \frac{\pi}{2} \cdot \frac{\text{sinc } B\tau}{\sin^{-1}(\text{sinc } B\tau)}. \quad (10)$$

This expression is plotted in Fig. 7 for a correlation radiometer having 20 MHz bandwidth.

For a hypothetical 1-bit L-band STAR radiometer with a 10 m span and a desired FOV of $\pm 35^\circ$, it can be inferred from (5) and (10) that the maximum-spacing visibility sample will suffer an extra 1.4 dB loss at the swath edge. This level of degradation does not necessarily preclude the use of 1-bit correlators for remote sensing STAR. But it does point out that if the effects of bandwidth spreading are not modeled, the visibility SNR at higher spatial frequencies—and thus the resolution of the synthesized beam—may be worse than expected.

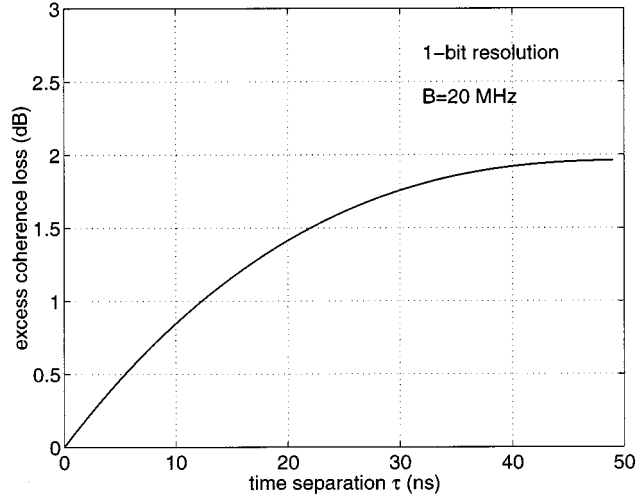


Fig. 7. Excess coherence loss in the fringe washing function. The vertical axis represents the loss incurred by using a 1-bit correlator as opposed to an ideal analog correlator, where the system bandwidth is set to 20 MHz for either case.

C. Other Sources of Converter Nonlinearity

Even after the effects of bandwidth spreading have been taken into account, there remain discrepancies between the measurements and modeled responses in Fig. 6(a). Data taken at 3.3 bit resolution appear to fit more closely with the theoretical curves at 1 or 2 bit resolution. One source of error may be differential nonlinearity exhibited by the A/D converter (i.e., nonuniform step size between quantization levels for each least-significant bit) [14], which introduces additional distortion and out-of-band harmonics in the quantized waveform. Also, there is an asymmetry in the measured fringe washing data that indicates a phase imbalance between the receiver channels; this may arise from a mismatch between the quantization transfer functions of the two digitizers. These nonideal effects merit further investigation and underscore that the end-to-end behavior of coarse resolution STAR correlators needs to be tested.

V. TECHNIQUE FOR ALLEVIATING DECORRELATION EFFECTS IN STAR

Section IV demonstrated that in digital correlation radiometers, quantization has the undesired effect of increasing the bandwidth and thus degrading the time-coherence between a pair of received signals. For STAR, nonzero bandwidth is in fact a general problem which places a fundamental limit on the spatial resolution capabilities of the sensor, even for ideal analog correlation hardware: Kraft has shown that, for a given bandwidth, the swath-edge resolution eventually reaches an absolute limit that cannot be surpassed by increasing the size of the array [15]. As next generation instruments following SMOS extend beyond a 10 m span to approach ≤ 10 km (mesoscale) resolutions for climate modeling, an alternative solution must be sought to alleviate fringe washing.

Ruf *et al.* have suggested splitting the receiver bandwidth into several smaller subbands before correlation and then individually transforming each visibility sample to reconstruct the image [16]. The smaller bandwidth naturally leads to an

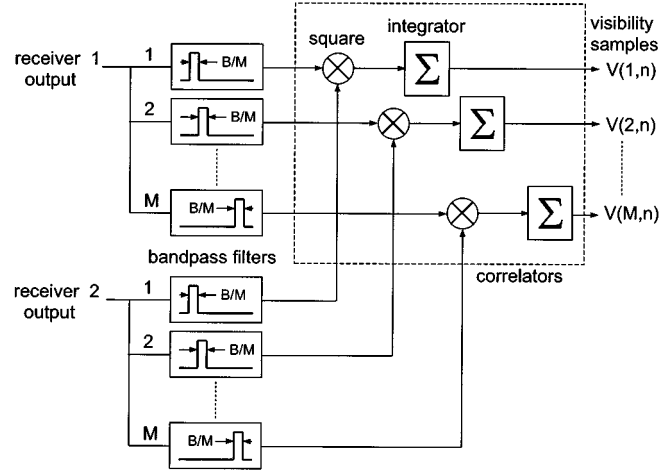


Fig. 8. Schematic of a band division correlation (BDC) radiometer. The received signals, each having bandwidth B , are divided evenly into M smaller bands to reduce decorrelation effects. In practice, the receiver outputs represent the pair of signals *after* A/D conversion, and all of the subsequent functions are implemented in digital processing to simplify the receiver design.

increased correlation time. Depending on the number of band divisions, fringe washing may be reduced significantly without compromising the overall bandwidth and sensitivity of the STAR radiometer. In this section, the band division correlation (BDC) concept shown in Fig. 8 is evaluated in the context of improving STAR's spatial frequency response.

The BDC receiver technique is applicable to either analog or digital hardware designs. It should be noted that in practice, though, a multi-channel correlator is vastly simpler to implement in digital hardware using FIR filter techniques than in analog hardware, which would require a bank of discrete microwave components. For DSDR applications, the two receiver outputs denoted in Fig. 8 can be treated as the digitized data streams following a pair of A/D converters.

In the following analysis, a one-dimensional STAR sensor in low Earth orbit with a desired resolution of 10 km will serve as a basis for comparing the point spread functions (PSFs) for conventional correlators and for the BDC architecture. A typical L-band soil moisture satellite is considered with the design parameters $f_0 = 1.41$ GHz, $B = 20$ MHz, altitude $h = 700$ km, and a field of view of $\theta = \pm 35^\circ$. To simplify the problem further, it is assumed that all antenna elements are isotropic, the array has a uniform amplitude distribution, and the Earth is flat across the FOV.

A. Beam Synthesis in a Conventional STAR Array

1) *Ideal Spatial Resolution and the Inverse Fourier Reconstruction Method:* Spatial resolution is first considered for the ideal case (where there is no fringe washing) by setting $r_w = 1$ and solving for the visibility response to a point source, located at $\mu = \mu_s$:

$$V(n, \mu_s) = \frac{e^{-j\pi n \mu_s}}{\sqrt{1 - \mu_s^2}}. \quad (11)$$

Note that in this case, (1) is just the Fourier transform of the modified brightness scene, defined as $T_B(\mu)/\sqrt{1 - \mu^2}$. There-

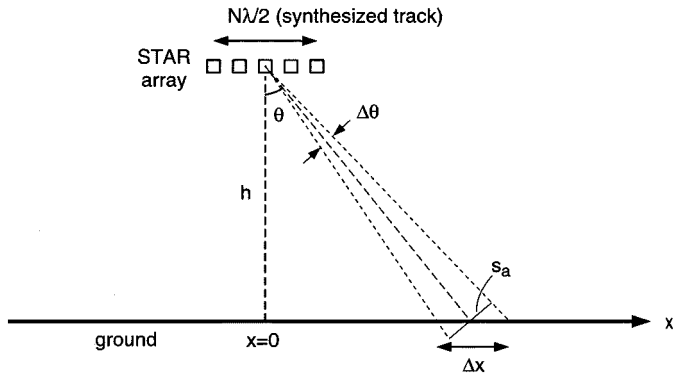


Fig. 9. Geometry for determining the spatial resolution in STAR.

fore the estimated image, \tilde{T}_B , is found by taking the inverse Fourier series of the visibility samples (F^{-1} reconstruction):

$$\begin{aligned}\tilde{T}_B(\mu) &= \sqrt{1-\mu^2} F^{-1} \{V(n)\} \\ &= \frac{1}{2} \sqrt{1-\mu^2} \sum_{n=-N}^N V(n) e^{j\pi n \mu}.\end{aligned}\quad (12)$$

Equation (12) describes the ideal PSF, which can be shown to have a main lobe centered at θ and an angular beamwidth (delimited by the first pattern nulls) of

$$\Delta\theta = \frac{\lambda}{D \cos \theta}, \quad (13)$$

where $D = N\lambda/2$ is the maximum dimension of the STAR array and the $\cos \theta$ term arises from aperture squint.

Fig. 9 illustrates the geometry for finding the size of the satellite's footprint at an angle θ away from nadir. At an altitude h , the sensor is a distance $h \sec \theta$ away from the pixel. Thus, the arc length of the main beam at ground level is

$$s_a = \frac{h \Delta\theta}{\cos \theta}, \quad (14)$$

and the projection on the ground becomes

$$\Delta x = \frac{s_a}{\cos \theta}. \quad (15)$$

Combining (13)–(15), the ideal spatial resolution is expressed as

$$\Delta x = \frac{2h}{N \cos^3 \theta}. \quad (16)$$

Therefore, to maintain at least 10 km resolution at the 35° swath edge would require a STAR array size of $N \approx 255$, or 27 m span, where the satellite's altitude is 700 km. This 27 m L-band STAR will be our reference model for evaluating the BDC architecture.

2) *Fringe Washing Degradation*: The tapering in visibility described in Section II can be included in calculations of the STAR point spread function. From (1) and (6), the visibility impulse response becomes

$$V(n, \mu_s) = \frac{r_w(n, \mu_s) e^{-j\pi n \mu_s}}{\sqrt{1-\mu_s^2}}. \quad (17)$$

As in the ideal case, the brightness estimate can be computed using the F^{-1} reconstruction:

$$\tilde{T}_B(\mu, \mu_s) = \frac{1}{2} \sqrt{\frac{1-\mu^2}{1-\mu_s^2}} \sum_{n=-N}^N r_w(n, \mu_s) e^{-j\pi n(\mu-\mu_s)}. \quad (18)$$

After cancelling imaginary components in the above series, the PSF becomes

$$\begin{aligned}\tilde{T}_B(\mu, \mu_s) &= \frac{1}{2} \sqrt{\frac{1-\mu^2}{1-\mu_s^2}} \\ &\times \left[1 + 2 \sum_{n=1}^N \text{sinc} \left(\frac{nB\mu_s}{2f_0} \right) \cos[\pi n(\mu-\mu_s)] \right].\end{aligned}\quad (19)$$

The solution in (19) will exhibit degraded resolution at large incidence angles, due to the behavior of the sinc function. This is not the best estimate of the original scene because F^{-1} reconstruction does not compensate for tapering of the grating lobe patterns in STAR.

3) *Inverse G-Matrix Reconstruction*: A numerical method is introduced to account for fringe washing and to minimize the error between estimated and actual brightness images. The system of N equations in (1) is expanded into a set of $2N+1$ real-valued visibility samples

$$V_l = \int_{-1}^1 g_l(\mu) T_B(\mu) d\mu, \quad l = 1, 2, \dots, 2N+1 \quad (20)$$

where the g functions represent the even and odd grating lobe patterns of the STAR sensor

$$g_l(\mu) = \begin{cases} r_w \left[\frac{(l-1)}{2}, \mu \right] \frac{\cos \left[\frac{\pi(l-1)\mu}{2} \right]}{\sqrt{1-\mu^2}}, & \text{for odd } l \\ r_w \left[\frac{l}{2}, \mu \right] \frac{\sin \left[\frac{\pi l \mu}{2} \right]}{\sqrt{1-\mu^2}}, & \text{for even } l. \end{cases} \quad (21)$$

The brightness scene T_B can be discretized into a set of P pixels spaced at uniform intervals on the μ axis. Then the system of visibility samples is written in matrix form as

$$V = GT \quad (22)$$

where

$$\begin{aligned}V &= \begin{bmatrix} V_1 \\ V_2 \\ \vdots \\ V_{2N+1} \end{bmatrix}, \quad T = \begin{bmatrix} T(\mu_1) \\ T(\mu_2) \\ \vdots \\ T(\mu_P) \end{bmatrix}, \\ G &= \begin{bmatrix} g_1(\mu_1) & g_2(\mu_2) & \cdots & g_1(\mu_P) \\ g_2(\mu_1) & g_2(\mu_2) & \cdots & g_2(\mu_P) \\ \vdots & \vdots & \ddots & \vdots \\ g_{2N+1}(\mu_1) & g_{2N+1}(\mu_2) & \cdots & g_{2N+1}(\mu_P) \end{bmatrix}\end{aligned}\quad (23)$$

with pixels located at

$$\mu_p = 2 \left(\frac{p-1}{P-1} \right) - 1 \text{ for } p = 1, 2, \dots, P. \quad (25)$$

The rows of the G -matrix in (24) make up the STAR basis functions (grating lobe patterns) for the various element-pair spac-

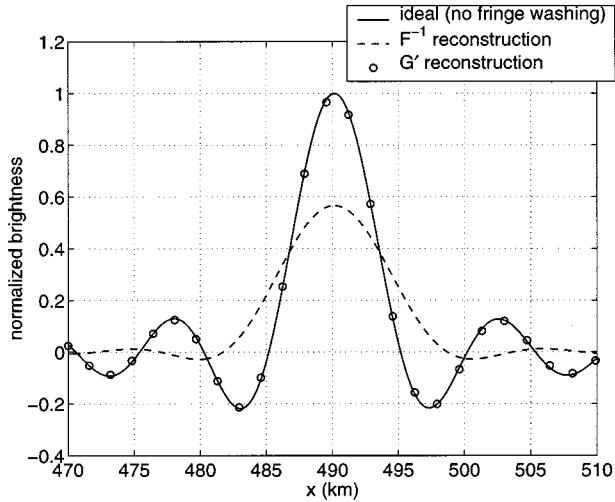


Fig. 10. Estimations of the 27 m STAR point spread function for a source located at 35° (490 km from nadir). The spatial frequency response is shown for the ideal (no fringe washing) case and for fringe washing cases where inverse Fourier and inverse G -matrix reconstruction techniques are applied. All PSFs are normalized to yield a peak value of 1 for a point source located at $x = 0$ km.

ings. It should be noted that the number of points P in the brightness vector is usually oversampled above $2N + 1$ so that the pixel size is fine enough to restore the image. Therefore, the inverse solution for (22) is under-determined. There is however a least-squares estimate of T , given by [17]

$$\tilde{T} = G^t V, \text{ where } G^t = G^t (GG^t)^{-1}. \quad (26)$$

G and G^t matrices were computed for the benchmark STAR with $N = 255$, using $P \approx 6N$ pixels. The PSF of the sensor can then be found by combining the visibility response in (17) with the G^t reconstruction technique in (26).

4) *SNR Degradation*: To gauge the effects of fringe washing, the image reconstruction techniques discussed so far can be applied to the most extreme case, where a point source is located on the border of the scene. In Fig. 10, the normalized point spread functions were computed for a source located 35° from nadir. For the ideal case where there is no fringe washing, the peak response is unity, and, as predicted by (16) for the benchmark STAR radiometer, the zero-crossing beam resolution is 10.0 km. Spatial resolution for the F^{-1} reconstruction case, which includes the effects of fringe washing in the visibility calculation, is significantly lower than the ideal response. The decorrelation between received signals in the array causes a 2.5 dB drop in the peak brightness level and a broadening of the beamwidth to 17.0 km. The pixels calculated using G^t reconstruction are also plotted with the other two curves for comparison. Here, the point spread function matches the ideal response exactly. As expected, G^t reconstruction takes into account and compensates for the tapered grating lobes at large element spacings.

Although G^t reconstruction yields the desired signal response, noise in the image will inevitably increase through this method. The estimated brightness in (26) is formed by adding a linear combination of inverse basis functions (columns of G^t) whose amplitudes tend to flare outward at oblique incidence angles. This flaring function is what allows the inversion

algorithm to compensate for fringe washing. However, no improvement in SNR is made by boosting a signal that has already incurred some loss; the noise floor will be raised during the processing, along with the brightness signal. Given that SNR is essentially the same for both F^{-1} and G^t cases, it follows from Fig. 10 that, as a consequence of fringe washing, the system sensitivity is reduced by 2.5 dB at $\theta = 35^\circ$.

B. Band-Slicing Technique

1) *Estimated Point Spread Function*: The BDC receiver in Fig. 8 can potentially remove the negative effects that arise from fringe washing. Let the original receiver bandwidth B be divided equally into M smaller slices with a bank of bandpass filters. For each subband processed by a correlator, the new fringe washing function will be dilated by a factor of M :

$$r_w(m, n, \mu) = \text{sinc}\left(\frac{nB\mu}{2Mf_m}\right) \quad (27)$$

where f_m is the center frequency of each subband

$$f_m = f_0 + \frac{B}{2M}[2m - (M + 1)] \quad (28)$$

and $m = 1, 2, \dots, M$ is the subband index. Equation (1) is then modified to yield a set of $M \times N$ subband visibility samples:

$$V(m, n) = \int_{-1}^1 \frac{1}{\sqrt{1-\mu^2}} T_B(\mu) r_w(m, n, \mu) \times \exp\left(\frac{-j\pi n f_m \mu}{f_0}\right) d\mu. \quad (29)$$

Using F^{-1} reconstruction, the impulse response for the m th subband is

$$\tilde{T}_B\{\text{mth band}\} = \frac{1}{2} \sqrt{\frac{1-\mu^2}{1-\mu_s^2}} \times \left[1 + 2 \sum_{n=1}^N \text{sinc}\left(\frac{nB\mu_s}{2Mf_m}\right) \cos\left[\frac{\pi n f_m (\mu - \mu_s)}{f_0}\right] \right]. \quad (30)$$

Each subband contains statistically independent noise, therefore the net brightness is found by summing the power over all subbands

$$\tilde{T}_B = \sum_{m=1}^M \tilde{T}_B\{m\}. \quad (31)$$

The normalized estimate of the point spread function is then

$$\tilde{T}_B(\mu, \mu_s) = \frac{1}{2N+1} \sqrt{\frac{1-\mu^2}{1-\mu_s^2}} \times \left[1 + \frac{2}{M} \sum_{m=1}^M \sum_{n=1}^N \text{sinc}\left(\frac{nB\mu_s}{2Mf_m}\right) \times \cos\left[\frac{\pi n f_m (\mu - \mu_s)}{f_0}\right] \right]. \quad (32)$$

The reconstructed image can be calculated for the benchmark STAR over a range of band divisions to assess the improvement in spatial resolution.

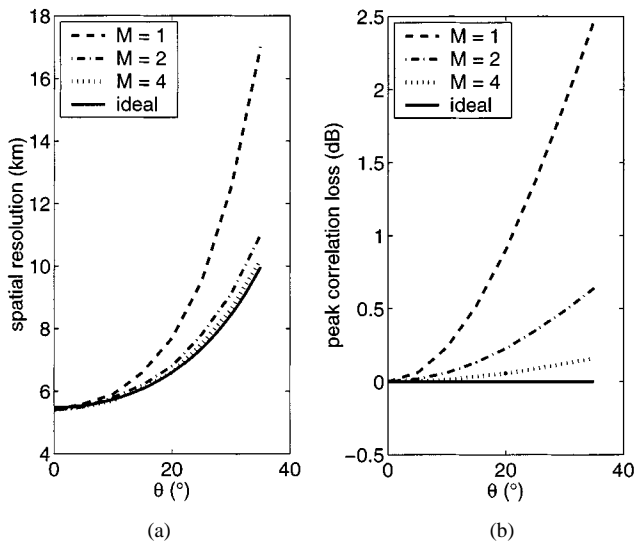


Fig. 11. (a) Spatial resolution versus incidence angle for a conventional STAR ($M = 1$), for a BDC instrument with $M = 2$ and 4 divisions, and for the ideal case. (b) Peak level correlation loss for the above cases.

2) *Numerical Results:* The BDC STAR point spread function in (32) was computed over the field of view for several different values of M . Fig. 11 shows a plot of the resulting spatial resolution and peak correlation loss compared to the ideal case. With just two subbands, there is already a significant improvement in resolution from 17.0 km to 11.0 km at 35° incidence; with $M = 4$, the resolution approaches a nearly ideal value of 10.2 km. Also, the correlation loss at the peak of the impulse response is reduced greatly with only a few band divisions. Compared to a conventional STAR with a 2.5 dB correlation loss, the BDC loss figure can be improved to 0.6 dB (for $M = 2$) or as low as 0.2 dB (for $M = 4$).

The STAR sensor considered here quickly converges to the “no fringe washing” case with a relatively small number of subband correlators. This implies that noise in high spatial frequency visibility samples can be reduced more effectively in a STAR sensor that employs BDC than in a sensor that used conventional correlators and G' post-processing.

Band-slicing was illustrated for the simple case of a uniform array distribution. But in a real world application, some amount of amplitude tapering would be designed into the reconstruction algorithm to reduce side lobe levels (e.g., ringing seen in the ideal response in Fig. 10) and to improve the efficiency of the synthesized beam. An actual 10 km resolution sensor would therefore require a maximum baseline greater than 27 m. The advantage gained through band-slicing is that, by giving the designer control over the shape of the fringe washing function, spatial resolution requirements can be satisfied over the entire field of view for an appropriate array size and number of band divisions.

The BDC method is especially well suited for present day STAR systems that transfer signal processing complexity away from analog hardware by digitizing the received brightness signals at IF or RF frequencies. Given the availability of DSP integrated circuits that run at 10^9 operations/second, it would be practical to develop L-band BDC radiometers having up to four frequency selective bands.

VI. CONCLUSIONS

Our analysis of the digital correlator performance in an L-band STAR radiometer has revealed an unexpected loss in fringe washing, even for pixels near the center of the field of view. The root cause of the excess loss of coherence was traced back to a bandwidth spreading phenomenon—that is, a broadening of the power spectrum that occurs after each brightness signal is digitized. Correlator designs with fewer bits of resolution naturally exhibit higher levels of nonlinearity and therefore suffer more from bandwidth spreading.

The fringe washing results inferred from experiments with our correlation DSDR carry a special significance for upcoming aperture synthesis missions. These data represent the first end-to-end fringe washing measurements to be documented for an L-band digital correlation radiometer operating in the protected radio astronomy band, with ~ 20 MHz of available bandwidth. Furthermore, the band spreading mechanism identified here would equally affect the performance of a single-bit, IF-sampling digital receiver, like the one proposed for the SMOS mission, as the fringe washing response is dependent on the system bandwidth but not on the detected carrier frequency. Without properly modeling the effects of bandwidth spreading, there will be an unanticipated loss of sensitivity in digital STAR arrays, especially at higher spatial frequencies, that leads to a broadening of the synthesized beam.

The negative effects of bandwidth spreading may be counteracted by increasing the number of bits used in the A/D converter and correlator sections of a digital STAR sensor. However, the added circuit complexity would tend to reduce the analog input bandwidth of the A/D sampler and could hamper the implementation of receiver architectures such as DSDR. A novel alternative is to keep the simple 1-bit converter design and instead apply a band-division correlation (BDC) processor *after* digitization, where the added circuit complexity is more affordable for circuit integration. Band-slicing is an effective way to increase the time-coherence of each processed brightness signal and thus alleviate fringe washing. An analysis of a 27 m BDC STAR sensor at L-band frequencies has shown that, using four subband processors, this technique will virtually eliminate decorrelation effects that would normally degrade spatial resolution.

REFERENCES

- [1] E. B. Fomalont, “Earth-rotation aperture synthesis,” *Proc. IEEE*, vol. 61, pp. 1211–1218, Sept. 1973.
- [2] D. M. Le Vine, “Synthetic aperture radiometer systems,” *IEEE Trans. Microwave Theory Tech.*, vol. 47, pp. 2228–2236, Dec. 1999.
- [3] D. M. Le Vine, A. J. Griffis, C. T. Swift, and T. J. Jackson, “ESTAR: A synthetic aperture microwave radiometer for remote sensing applications,” *Proc. IEEE*, vol. 82, pp. 1787–1801, Dec. 1994.
- [4] T. J. Jackson, D. M. Le Vine, A. Y. Hsu, A. Oldak, P. J. Starks, C. T. Swift, J. D. Isham, and M. Haken, “Soil moisture mapping at regional scales using microwave radiometry: The southern great plains hydrology experiment,” *IEEE Trans. Geosci. Remote Sensing*, vol. 37, pp. 2136–2151, Sept. 1999.
- [5] K. Rautiainen, R. Butora, T. Auer, I. Mononen, J. Salminen, S. Tauriainen, M. Hallikainen, J. Uusitalo, and P. Jukkala, “The Helsinki University of Technology/Ylinen electronics airborne L-band interferometric radiometer,” in *Proc. IGARSS 2000*, vol. 7, Honolulu, HI, July 2000, pp. 2978–2980.

- [6] I. Corbella, F. Torres, A. Camps, J. Bará, N. Duffo, and M. Vall-Illouera, "L-band aperture synthesis radiometry: Hardware requirements and system performance," in *Proc. IGARSS 2000*, vol. 7, Honolulu, HI, July 2000, pp. 2975–2977.
- [7] A. Borges, A. Solana, M. A. Plaza, J. A. Sanz, and Q. Garcia, "The MIRAS demonstrator pilot project," in *Proc. IGARSS 2000*, vol. 7, Honolulu, HI, July 2000, pp. 2972–2974.
- [8] S. Weinreb, "Digital radiometer," *Proc. IEEE*, vol. 49, p. 1099, June 1961.
- [9] B. F. C. Cooper, "Correlators with two-bit quantization," *Aust. J. Phys.*, vol. 23, pp. 521–527, 1970.
- [10] J. B. Hagen and D. T. Farley, "Digital-correlation techniques in radio science," *Radio Sci.*, vol. 8, no. 8, pp. 775–784, Aug.–Sept. 1973.
- [11] B. Laursen and N. Skou, "Synthetic aperture radiometry evaluated by a two-channel demonstration model," *IEEE Trans. Geosci. Remote Sensing*, vol. 36, pp. 822–832, May 1998.
- [12] P. Z. Peebles, Jr., *Probability, Random Variables, and Random Signal Principles*, 3rd ed: McGraw-Hill, 1993, ch. 7, pp. 209–214.
- [13] M. A. Fischman and A. W. England, "Sensitivity of a 1.4 GHz direct-sampling digital radiometer," *IEEE Trans. Geosci. Remote Sensing*, vol. 37, pp. 2172–2180, Sept. 1999.
- [14] P. Horowitz and W. Hill, *The Art of Electronics*, 2nd ed. Cambridge, U.K.: Cambridge Univ. Press, 1989, ch. 9, pp. 614–615.
- [15] U. R. Kraft, "Spaceborne synthetic aperture interferometric radiometers for global monitoring of the earth," in *Proc. IGARSS'91*, vol. II, Helsinki, Finland, June 1991, pp. 971–974.
- [16] C. S. Ruf, C. T. Swift, A. B. Tanner, and D. M. Le Vine, "Interferometric synthetic aperture microwave radiometry for the remote sensing of the earth," *IEEE Trans. Geosci. Remote Sensing*, vol. 26, pp. 597–611, Sept. 1988.
- [17] A. B. Tanner and C. T. Swift, "Calibration of a synthetic aperture radiometer," *IEEE Trans. Geosci. Remote Sensing*, vol. 31, pp. 257–267, Jan. 1993.



Mark A. Fischman (S'95–M'01) received the B.S. degree in electrical engineering from the California Institute of Technology, Pasadena, in 1989, and the M.S. and Ph.D. degrees in electrical engineering from the University of Michigan, Ann Arbor, in 1996 and 2001, respectively.

He worked at the Sony Corporation television development groups, Tokyo, Japan and Pittsburgh, PA, from 1989 to 1995. In 2001, he joined the Radar Science and Engineering Section at the Jet Propulsion Laboratory, Pasadena, where he is currently developing

the on-board processing and adaptive scanning control systems for the Next-Generation Precipitation Radar satellite instrument. His research interests include the development of advanced digital receivers, phased-array and aperture synthesis techniques for microwave radar and radiometry.



Anthony W. England (M'87–SM'89–F'95) received the Ph.D. degree in geophysics from the Massachusetts Institute of Technology, Cambridge, in 1970.

He is Professor of electrical engineering and computer science and Professor of atmospheric, oceanic, and space sciences at the University of Michigan, Ann Arbor. His research has included scattering theory applied to the microwave brightness of the Earth and planets, and the development and use of ice-sounding radar for the study of glaciers in Alaska and Antarctica. His current research focuses upon developing and calibrating Land-Surface Process/Radiobrightness (LSP/R) models of land-atmosphere energy and moisture fluxes for the North American prairie and the Arctic, and upon developing new radiometer technologies. He has been Co-Investigator for the Apollo 17 Surface Electrical Properties experiment, and Co-Investigator on Shuttle Imaging Radar –A and –C experiments. He was a Scientist-Astronaut during two periods with NASA, where he served as Mission Scientist for Apollo's 13 and 16, Mission Specialist on the Spacelab 2 flight in 1985, and Space Station Program Scientist in 1986–1987. He was a Research Geophysicist and Deputy Chief of the Office of Geochemistry and Geophysics with the U.S. Geological Survey from 1972 through 1979, and a Visiting Adjunct Professor at Rice University, Houston, TX, in 1987 before joining the University of Michigan in 1988. He has been an Associate Editor for the *Journal of Geophysical Research*.

Dr. England is a member of the Administrative Committee of the IEEE Geoscience and Remote Sensing Society, a member of the National Research Council's Space Studies Board, and chair of several federal committees concerned with science and technology policy. He is a member of the American Geophysical Union.



Christopher S. Ruf (S'85–M'87–SM'92–F'01) received the B.A. degree in physics from Reed College, Portland, OR, and the Ph.D. degree in electrical and computer engineering from the University of Massachusetts, Amherst.

He is an Associate Professor of atmospheric, oceanic and space sciences and electrical engineering and computer science at the University of Michigan, Ann Arbor. He has worked previously in production engineering for Intel Corporation as a Technical Staff Member at the NASA Jet Propulsion

Laboratory, Pasadena, CA, and as a member of the faculty at Pennsylvania State University, University Park. During 2000, he was a Guest Professor at the Technical University of Denmark, Lyngby. His research interests involve ground, air and space borne passive microwave remote sensing technology, systems and applications.

Dr. Ruf has received three NASA Certificates of Recognition and three NASA Group Achievement Awards, as well as the 1997 GRS-S Transactions Prize Paper Award and the 1999 IEEE Judith A. Resnik Technical Field Award. He is a member of the AGU, AMS, and URSI Commission F and is chairman of the IEEE GRS Technical Committee on Frequency Allocations for Remote Sensing. He is a past Editor of the IEEE GRS-S Newsletter, past Guest Editor and Associate Editor for *Radio Science*, and current Associate Editor of the IEEE TRANSACTIONS ON GEOSCIENCE AND REMOTE SENSING.